I-EDU GROUP

Article

Electronic and Transport Properties of Ag3PO4 as a basis for catalytic applications

Olga Galkina *[1], **Shavkat Mamatkulov** [1], **L.S. Khoroshko** [2,3]

[1] Laboratory of multifunctional materials, Institute of Material Science, Tashkent, 100084, Uzbekistan
[2] Laboratory of Energy-Efficient Materials and Technologies, Belarusian State University, Minsk, 220030, Belarus
[3] Center 4.11 «Nanoelectronics and advanced materials», Belarusian State University of Informatics and Radioelectronics,Minsk, 220013, Belarus
helga93rr@mail.ru (O.G.), mi-shavkat@yandex.com(Sh.M.), khoroshko@bsu.by (L.Kh.)
* Correspondence: helga93rr@mail.ru; Tel.: +998 97 7506792 (O.G.)

Abstract:
The electronic, structural and transport properties of the semiconductor silver phosphate Ag_3PO_4 have been investigated using first-principles methods. The influence of deformation on the band gap width, effective masses of charge carriers, their lifetimes and mobilities, elastic modulus constants, and deformation potentials has been studied. It has been shown that silver phosphate with a cubic crystal lattice is a semiconductor with both direct and indirect transitions (energy gaps of 2.54 eV and 2.47 eV respectively), that is consistent with experimental data. It has been established that the effective masses of electrons are approximately three times smaller than those of holes, and the electron lifetime (21.8 fs) significantly exceeds the hole one (2.9 fs), indicating the electronic conductivity of Ag_3PO_4. With increasing deformation, the effective mass of electrons rises, while the effective mass of holes remains practically unchanged under compressive deformation, decreases under tensile deformation, and then returns to the initial value with further increase in tension. Electron mobility is maximum in the absence of deformation ($66.14\,\mathrm{cm}^2/(\mathrm{V}\cdot\mathrm{s})$) and significantly decreases when deformation is applied. The obtained results can be used in the design of photocatalytic and strain-sensing materials containing silver phosphate.

Keyword: silver phosphate, deformation potential theory, effective mass, lifetime, binding energy.

Quoting: Olga Galkina, Shavkat Mamatkulov, L.S. Khoroshko. Electronic and Transport Properties of Ag3PO4 as a basis for catalytic applications. **2025**, 2, 2, 5. https://doi.org/

Received: 10.03.2025
Corrected: 18.03.2025
Accepted: 25.04.2025
Published: 30.04.2025

Introduction

Intensive industrial development and urbanization are exacerbating environmental sustainability issues, necessitating the search for alternative energy sources. Key challenges include the removal of organic pollutants from water systems and the efficient conversion of solar energy into chemical energy. In this context, particular attention in recent years has been paid to semiconductor photocatalytic materials capable of simultaneously degrading toxic organic compounds and photocatalytically generating hydrogen without producing carbon-containing emissions [1–3]. Traditional photocatalysts, such as TiO_2 [4,5] and ZnO [6–8], are active primarily under the influence of ultraviolet radiation, which constitutes only a small fraction of the solar spectrum [9], raising the demand for new catalysts sensitive to the visible spectrum. Such compounds include $BiVO_4$ [10,11], WO_3 [13–15], BiOI [16,17], CdS [18–20], $ZnIn_2S_4$ [21,22], g-C_3N_4 [23,24] and silver halides AgX ($X = \mathrm{Cl, Br, I}$) [25,29]. Among them, silver-containing compounds, namely Ag_3PO_4 [30,31], Ag_2CO_3 [32,33], Ag_3VO_4 [34–36], $AgSbO_3$ [37,38], and $Ag_6Si_2O_7$ [39], are quite promising materials for photocatalysis due to their narrow band gap and high photoactivity under visible light, but are susceptible to degradation under prolonged illumination and photocorrosion.

The use of conductive matrices and carriers (graphene, carbon nanotubes, highly conductive oxides) accelerates charge transport and prevents electron accumulation at Ag^+ centers. Controlled formation of nanostructures (nanoparticles, nanowires, nanofilms) increases the active surface area and enables the rational management of defects affecting photostability. Thus, fundamental studies of the electronic structure, transport properties, and the influence of external factors for Ag_3PO_4

are of particular importance essential for reducing its instability and mitigating photocorrosion processes during use. A thorough understanding of these characteristics and the mechanisms of chemical processes in the presence of Ag_3PO_4 is key to the creation of modified composite systems characterized by increased stability and capable of combining high photoactivity with a long service life.

In this study, using first-principles methods (DFT, GGA/PBE with Hubbard corrections), a comprehensive study of the electronic structure, mechanical stability, and transport properties of the cubic Ag_3PO_4 structure is conducted. For the first time, the effect of deformation on the band gap and effective masses of charge carriers is analyzed in detail. Prospects for further modification of the material aimed at optimizing its photoactivity and operational stability are discussed.

Materials and Methods

Ab initio calculations were performed using the Quantum Espresso package [41] using optimized norm-conserving Vanderbilt pseudopotentials (ONCVPSP) [42] and the PBE (Perdew–Burke–Ernzerhof) exchange-correlation functional [43] within the DFT GGA+U method [44]. The kinetic energy and charge density cutoffs were chosen to be 680 eV and 5440 eV, respectively, while the Brillouin zone was chosen using a $6 \times 6 \times 6$ grid according to the Monkhorst–Pack scheme. The electron-valence configurations are given by Ag – [Kr] $4d^{10}5s^1$, O – [He] $2s^2 2p^4$, P – [Ne] $3s^2 3p^3$. The Hubbard corrections U were chosen as follows: Ag($4d$) = 7.2 eV, O($2p$) = 5.0 eV, P($3p$) = 5.0 eV. The space group of the crystal is $P4_3n$. The body-centered cubic unit cell of Ag_3PO_4 ($a = 6.014$ Å), including 16 atoms, was taken from the Materials Project database [**?**].

According to the deformation potential theory proposed by Bardeen and Shockley [46], the mobility of charge carriers in a bulk material is determined by the formula:

$$\mu_e^{3D} = \frac{2^{3/2}\pi^{1/2}}{3}\frac{c^3 D_\hbar^4 e}{E_l^2 m^{*\,5/2}(k_B T)^{3/2}} \tag{1}$$

where C^{3D} is the elastic modulus constant, E_l is the strain potential constant, T is the temperature, and m^* is the electron effective mass.

The strain potential constant E_l is proportional to the shift of the valence band for a hole or the conduction band for an electron caused by the applied voltage and is defined as:

$$E_l = \frac{d(E - E_0)}{d(\ln V)} \tag{2}$$

where E is the LUMO/HOMO energy as a function of stress, and V is the lattice volume.

The elastic modulus constant C^{3D} expresses the change in total energy E under deformation δ, divided by the equilibrium volume V_0, and is expressed by the formula:

$$C^{3D} = \frac{\partial^2 E}{\partial \delta^2} \Big/ V_0 \tag{3}$$

The effective masses of an electron or hole are calculated according to the formula:

$$m^* = \frac{\hbar^2}{\dfrac{\partial^2 E}{\partial k^2}} \tag{4}$$

where E is the charge carrier energy, and k is the wave vector. To characterize the efficiency of electron–hole separation, the following ratio is calculated:

$$D = \frac{m_h^*}{m_e^*} \tag{5}$$

where is the effective mass of a hole, and is the effective mass of an electron. The higher the value of D, the better the charge separation.

Results

In our work, we considered Ag_3PO_4 in the space group $P4_3n$ with two formula units within a cell size of 6.0141 Å (Figure 1).

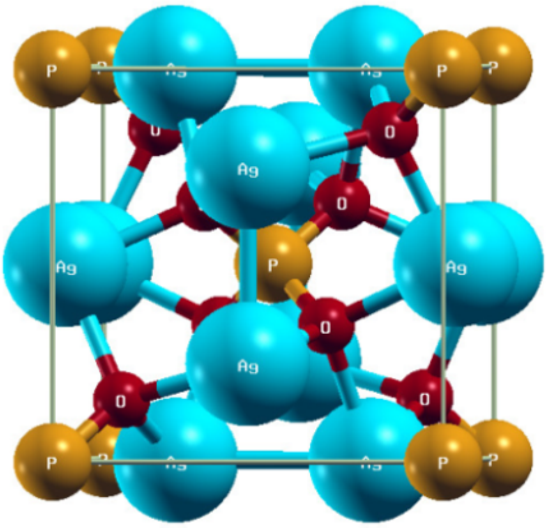

Figure 1. Spatial structure of Ag3PO4 P43n.

ONCVPSP pseudopotentials with Hubbard corrections were used to optimize the lattice geometry and cell dimensions. The optimization results and comparison with experimental data from the literature are presented in Table 1.

The body-centered cubic lattice of Ag_3PO_4 consists of PO_4 and AgO_4 tetrahedra. Each Ag and P atom is coordinated by four O atoms, while each O atom is coordinated by three Ag atoms and one P atom. Due to the higher electronegativity of P compared to Ag, a strong distortion of the AgO_4 tetrahedra occurs, which is reflected in the calculation results: after optimization with ONCVPSP pseudopotentials, a noticeable decrease in bond lengths and the lattice parameter is observed.

Table 1. Comparison of experimental and calculated structural parameters of the Ag3PO4 cell

Ag-O bond length	P-O bond length	Ag-Ag bond length	O-O bond length	Lattice parameter	Source
2.36	1.56	3.00	-	6.00	Exp. [47]
2.38	1.55	-	3.47	6.03	Exp.[48]
2.37	1.55	3.01	3.47	6.01	This work (before optimization)
2.20	1.53	2.82	3.19	5.64	This work (after optimization)

For the optimized configuration of Ag_3PO_4, the band structure was calculated and the projected density of states (PDOS) was analyzed, as shown in Figure 2. The obtained results are consistent with published studies, in which Ag_3PO_4 has direct and indirect transitions. The direct transition is observed at the Γ point with $E_{\text{gap}} = 2.54$ eV, and the indirect transition is between the M and Γ points with $E_{\text{gap}} = 2.47$ eV. According to experimental data, these parameters are 2.36 eV and 2.43 eV, respectively [40]. The observed dispersion of the conduction band indicates a lower effective electron mass compared to the effective hole mass, and, accordingly, higher electron mobility as a charge carrier.

Based on the PDOS plot, which demonstrates the energy distribution of electron levels, the valence band is formed mainly by localized Ag $4d$ states with clear peaks, as well as delocalized O $2p$ states.

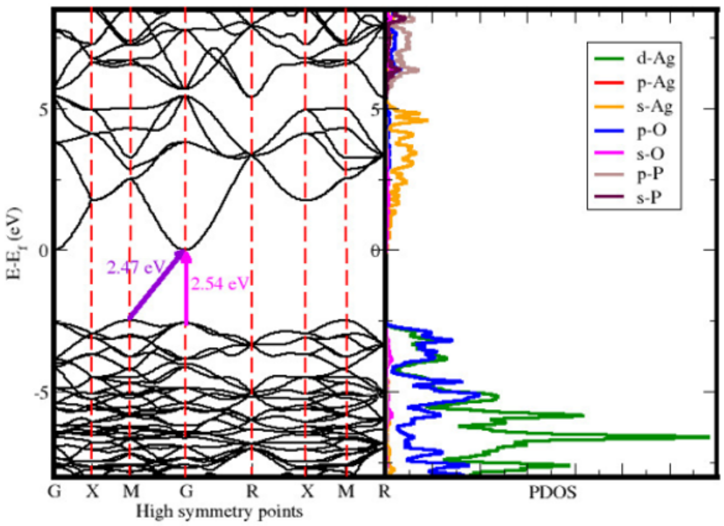

Figure 2.

Fig. 2. Band structure of Ag3PO4 and PDOS analysis.

The conduction band consists predominantly of diffuse and weakly defined Ag 5s states, located in the range of 2.5–7.5 eV. The Ag 5p states are highly delocalized throughout the energy range studied. The P 3s states of phosphorus in the conduction band are more localized than the 3p states.

To calculate the deformation potential constant E_l, the crystal lattice was subjected to isotropic expansion and compression of 5%. To determine the deformation potential constants, a linear approximation of the dependence of the LUMO and HOMO level energies on the relative change in the crystal cell volume was performed (Figure 3). The negative deformation potential constants for LUMO and HOMO, -23.97 eV and -21.67 eV, respectively, indicate a decrease in the energy level of the valence band and conduction band edges with increasing volume (stretching). Thus, the band structure exhibits moderate and nearly symmetric sensitivity to deformation.

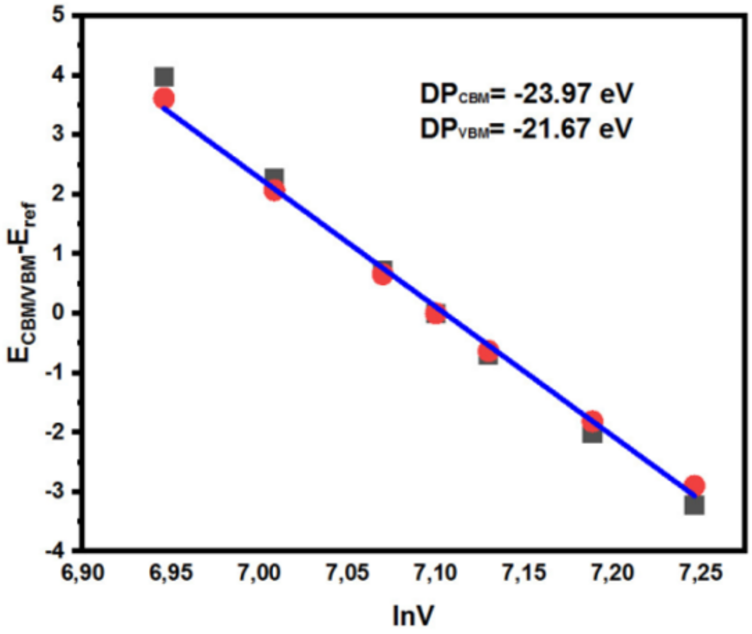

Figure 3.

Fig. 3. Energy of LUMO and HOMO levels as a function of the logarithm of the volume during deformation.

The elasticity constant or C3D was determined using the thermo_pw.x module of the Quantum Espresso package by approximating the dependence of the total energy of the system on a third-degree polynomial – the Birch–Murnagen equation of state (EOS) of the third order (BM3) [49]:

$$E(V) = E_0 + \frac{9V_0B_0}{16}\left\{\left[\left(\frac{V_0}{V}\right)^{2/3} - 1\right]^3 B_0' + \left[\left(\frac{V_0}{V}\right)^{2/3} - 1\right]^2 \left[6 - 4\left(\frac{V_0}{V}\right)^{2/3}\right]\right\} \tag{6}$$

where $E(V)$ is the energy of the system at volume V, E_0 is the equilibrium energy at volume V_0, B_0 is the bulk modulus or elasticity constant, B_0' is the derivative of the bulk modulus with respect to pressure, and V is the current volume.

The elastic modulus constant for our system was found to be 158.02 GPa for a cell volume of 179.57 Å, while Yang Lu et al. [50] obtained a value of 101.29 GPa for a cubic cell with a volume of 217.47 Å.

This difference in elasticity constant values may be due to stronger interatomic interactions in the smaller cell volume combined with the greater rigidity of the structure itself. In a small-volume cell, repulsive forces increase and deformation resistance increases, which in turn leads to an increase in the elastic modulus constant.

Table 2 shows the transport characteristics of Ag_3PO_4. The electron and hole effective masses are 0.58 m_0 and 2.51 m_0, respectively, and are comparable with previously published results [51,52]. The hole effective masses are approximately three times greater than the electron effective mass, indicating that electron conductivity in Ag_3PO_4 is preferential to hole conductivity, despite Ag_3PO_4 being a traditional p-type semiconductor. This can be explained by the fact that our calculations assume an ideal crystal structure, in which electrons are more easily excited and more mobile. However, a real crystal contains Ag^+ vacancies and holes, which are responsible for hole conductivity.

Table 2. Calculated effective masses (m*) of electrons and holes and the ratio of their effective masses, D

Deformation, %	Egap, eV	m$^*_e$	m$^*_h$	D
-5	2.82	0.92	2.40	2.62
-3	2.68	1.01	2.43	2.41
-1	2.53	0.97	2.46	2.54
0	2.46	0.58	2.51	4.34
1	2.44	0.86	1.88	2.18
3	2.27	0.88	2.49	2.81
5	2.18	0.82	2.60	3.18

Table 2 and Figure 4 present the results of studying the effect of deformation on the band structure of Ag_3PO_4. Under cell compression, the band gap increases from 2.46 eV to 2.82 eV, which reduces the probability of excitation of electrons in the conduction band and contributes to a decrease in sensitivity to the visible spectrum. Conversely, under maximum cell stretching, the band gap reaches a minimum value of 2.18 eV, which shifts the absorption edge to longer wavelengths and leads to an increase in the ability to absorb visible light. However, under large deformations, a decrease in band dispersion is also observed, which negatively affects the transport properties of the material.

The effective mass of an electron in the absence of deformation is $m_e^* \approx 0.58\,m_0$, indicating its high mobility. Under both compression and stretching, the mass increases to $\sim$ 0.82–1.0 m_0, as a result of which electron mobility naturally decreases. For holes, the mass remains significantly greater than that of electrons and remains virtually constant ($\approx$ 2.4–2.6 m_0), resulting in weak hole conductivity regardless of the degree of deformation. The coefficient D, as expected, has its highest value of 4.34 in the absence of stress.

Table 3. Calculated constants of the deformation potential E_l and elasticity C^{3D}, charge carrier mobility μ, and their lifetime τ

Deformation, %	$\Delta E_i(e)$, eV	$\Delta E_i(h)$, eV	C_{3D}, GPa	μ_e, $\mathrm{cm^2/(V \cdot s)}$	μ_h, $\mathrm{cm^2/(V \cdot s)}$	τ_e, fs	τ_h, fs
-5	-23.94	-21.67	158.02	20.95	2.32	10.92	3.15
-3				16.51	2.24	9.46	3.09
-1				18.40	2.17	10.10	3.04
0				66.14	2.06	21.76	2.94
1				24.39	4.22	11.96	4.52
3				22.95	2.11	11.53	2.98
5				27.96	1.89	12.98	2.79

Table 3 presents the mechanical and transport characteristics of Ag_3PO_4. The electron mobility is $\mu_e = 66.14\ \mathrm{cm^2/(V\,s)}$ at zero strain, which is the maximum value, and at ±5% the mobility decreases by 3–6 times (to 20–28 $\mathrm{cm^2/(V\,s)}$). The hole mobility is low (2–4 $\mathrm{cm^2/(V\,s)}$) and responds weakly to strain. The calculated values for μ for our experimental configuration are greatly overestimated relative to the data published by Sinha et al. ([53], 0.041 $\mathrm{cm^2/(V\,s)}$ for electrons and 0.009 $\mathrm{cm^2/(V\,s)}$ for holes), but the trends remain the same – electrons are the majority charge carriers. In the absence of deformation, the electron lifetime is $\tau_e \approx 21.8$ fs, which significantly exceeds the value obtained for holes ($\tau_h \approx 2.9$ fs). Under compression, τ_e drops to ~ 10 fs, while τ_h increases slightly. The longer electron lifetime is consistent with previous conclusions about their major contribution to the photocurrent; however, the high mobility of majority carriers also accelerates the recombination of electron–hole pairs, which shortens the effective charge separation time.

Thus, deformation alters the balance: compression increases the E_g value, reduces mobility, but can improve resistance to photocorrosion; stretching, in turn, reduces E_g and improves absorption, but reduces transport properties.

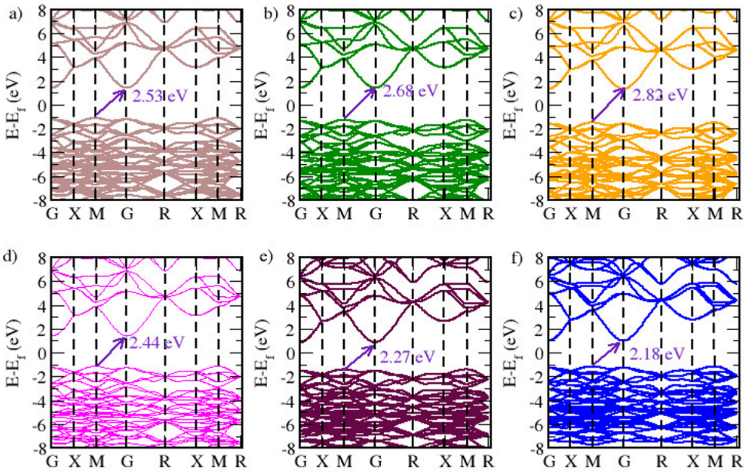

Figure 4. Change in the zone structure when applying deformation under compression (a) -1%, b) -3%, c) -5%) and tension (d) 1%, e) 3%, f) 5%).

The binding energy E_{bind} was determined using the formula [54]:

$$E_{\mathrm{bind}}(N) = E(N) - E(N-1) - E_{\mathrm{at}} \tag{7}$$

where $E(N)$ and $E(N-1)$ is the total energy of the system of atoms and the energy of the system of atoms $(N-1)$, E_{at} is the energy of a free atom.

As can be seen from Table 4, the phosphorus atom has the highest binding energy, forming strong covalent bonds with oxygen atoms. The silver atom is most weakly bound to the crystal lattice, which may explain its increased mobility, leading to the formation of Ag vacancies. Thus, the

Ag_3PO_4 structure is stabilized primarily by PO_4 tetrahedra, while Ag atoms are thermodynamically less stable.

Table 4. Binding energies in the Ag3PO4 system

System type	E, eV	E_{bind}, eV
Ag_3PO_4	-29229.53	
Ag	-4211.82	-2.67
P	-179.54	-22.18
O	-443.28	-5.04
Ag_2PO_4	-25015.04	
Ag_3O_4	-29027.81	
Ag_3PO_3	-28781.21	

We determined the absolute values of the position of the edges of the zones (E_{CB} and E_{VB}) based on the use of electronegativity according to Mulliken [55]:

$$E_{CB} = \chi - E_c - \frac{1}{2}E_g \tag{8}$$

$$E_{VB} = E_{CB} + E_g \tag{9}$$

$$\chi = \left[\chi(A)^a \chi(B)^b \chi(C)^c\right]^{1/(a+b+c)} \tag{10}$$

where E_{CB} and E_{VB} are the energies of the conduction-band and valence-band edges, respectively, E_g is the band gap, and χ is the absolute electronegativity of the semiconductor. Here, $\chi(A)$, $\chi(B)$, and $\chi(C)$ denote the electronegativities of atoms A, B, and C, respectively, while E_c is the energy of free electrons on the hydrogen scale ($\sim$ 4.5 eV).

The absolute electronegativity of Ag_3PO_4 is calculated to be 5.96 eV, whereas the conduction-band minimum (E_{CB}) and valence-band maximum (E_{VB}) are located at 0.23 eV and 2.69 eV, respectively. Since E_{CB} is more positive than the reduction potential of H^+/H_2 (0 eV), Ag_3PO_4 is incapable of reducing hydrogen and, therefore, cannot participate in the hydrogen evolution reaction (HER). In contrast, E_{VB} is significantly higher than the oxidation potential of water to oxygen (O_2/H_2O, +1.23 eV), enabling Ag_3PO_4 to oxidize water to produce O_2 as well as to oxidize organic compounds, particularly in photocatalytic cycles. The obtained results are in good agreement with previous theoretical studies [52,57] and available experimental data [40].

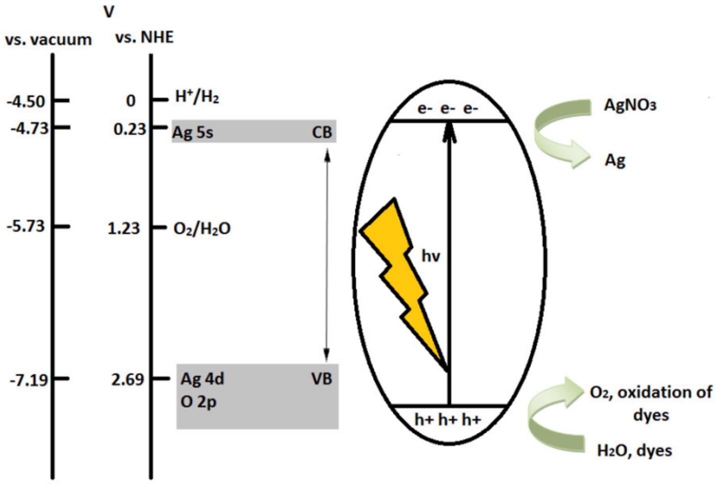

Figure 5. Results of calculations of the positions of the valence band (VB) and conduction band (CB).

Conclusions

We conducted a comprehensive study of the electronic structure, mechanical stability, and transport properties of silver phosphate Ag_3PO_4 in the cubic modification using the DFT method with Hubbard corrections. It was shown that the studied material has a narrow band gap and is highly sensitive to deformation. Analysis of the transport characteristics and the effects of deformation indicates the predominance of electronic conductivity, which decreases sharply under mechanical stress. The identified high mobility of charge carriers not only ensures efficient transport but also leads to rapid recombination of electron–hole pairs. Analysis of the binding energies revealed that the Ag_3PO_4 structure is stabilized by PO_4 tetrahedra, while Ag atoms are more weakly bound to the crystal lattice, explaining the tendency to form silver vacancies. The positions of the energy band edges confirm the ability of Ag_3PO_4 to exhibit oxidizing properties, particularly in processes such as oxygen generation and the decomposition of organic compounds. The obtained results provide the basis for further in-depth study of Ag_3PO_4 with the aim of structural optimization aimed at increasing its resistance to photocorrosion and improving its performance in composite photocatalysts. The obtained dependences of the electronic properties of silver phosphate on tension and compression may find application in the design of small strain detectors.

Authors' contribution.

Conceptualization,Sh.M. and L.Kh.;methodology,Sh.M.;software,O.G.;validation, O.G.; formal analysis,L.Kh.; investigation,O.G.;resources,Sh.M.;data curation,O.G.;writing—original draft preparation,O.G.; writing—review and editing, Sh.M. and L.Kh.; visualization, O.G.; supervision, Sh.M. and L.Kh.; project administration, L.Kh.; funding acquisition, Sh.M. All authors have read and agreed to the published version of the manuscript.

Funding source.

This research was funded by the Ministry of Higher Education, Science, and Innovation of the Republic of Uzbekistan No. FL-7923051799.

Ethics approval.

Since this study does not involve human or animal subjects, ethical review and approval is not required. Therefore, ethical approval does not apply to research.

Consent for publication

Human participants were not involved in this study. For this reason, informed consent is not required.

Data Availability Statement

All computational data confirming the results presented in this article are held by the authors and presented within the article in the form of the main text and image/table. Additional information can be obtained from the author(s)based on a reasoned query.

Acknowledgments

The authors thank the team of the Institute of Materials Science providing technical assistance in the implementation of this research.

Conflict of interest

The authors declare no conflicts of interest.

Abbreviations

DFT	Density Functional Theory
GGA	Generalized Gradient Approximation
PBE	Perdew–Burke–Ernzerhof functional
ONCVPSP	Optimized norm-conserving Vanderbilt pseudopotentials
U	Hubbard parameter
HOMO	Highest Occupied Molecular Orbital
LUMO	Lowest Unoccupied Molecular Orbital
C^{3D}	Elastic modulus constant
E_I	Strain potential constant
D	Efficiency of electron-hole separation

DOS	Density of States
PDOS	Projected Density of States
EOS	Birch–Murnagen equation of state
E_{bind}	Binding energy
VBM	Valence Band Maximum
CBM	Conduction Band Minimum

References

[1] A.K.D. Alsukaibi. Various Approaches for the Detoxification of Toxic Dyes in Wastewater. Processes,2022, 10, 1968. https://doi.org/10.3390/pr10101968.

[2] M.Pirilä,M. Saouabe, S.Ojala, B.Rathnayake, F.Drault, A.Valtanen, Mika Huuhtanen,Rachid Brahmi, R. L. Keiski. Photocatalytic Degradation of Organic Pollutants in Wastewater. Topics in Catalysis,2015, 58(14-17), 1085–1099. https://doi.org/10.1007/s11244-015-0477-7.

[3] A. B. Djurišić, Y. He, A. M. C. Ng. Visible-light photocatalysts: Prospects and challenges. APL Materials, 2020, 8(3), 030903. https://doi.org/10.1063/1.5140497.

[4] I. Abdelfattah, A.M. El-Shamy. A comparative study for optimizing photocatalytic activity of TiO2-based composites with ZrO_2, ZnO, Ta_2O_5, SnO, Fe_2O_3, and CuO additives. Sci.Rep., 2024, 14, 27175. https://doi.org/10.1038/s41598-024-77752-5.

[5] Ayush Badoni, Sahil Thakur, Narayanasamy Vijayan, Hendrik Christoffel Swart, Mikhael Bechelany, Zhengsen Chen,Shuhui Sun,Qiran Cai, Ying Chen and Jai Prakash. Recent progress in understanding the role of graphene oxide, TiO2 and graphene oxide-TiO2 nanocomposites as multidisciplinary photocatalysts in energy and environmental applications. Catal. Sci. Technol., 2025,15, 1702-1770

[6] Ngoc Thinh Nguyen, Van Anh Nguyen. Synthesis, Characterization, and Photocatalytic Activity of ZnO Nanomaterials Prepared by a Green, Nonchemical Route, Journal of Nanomaterials,2020,Volume 2020, 1-8 pages. https://doi.org/10.1155/2020/1768371.

[7] K.Singh, Nancy, M.Bhattu, G. Singh,N. M. Mubarak,J. Singh. Light-absorption-driven photocatalysis and antimicrobial potential of PVP-capped zinc oxide nanoparticles. Sci.Rep.,2023, 13, 13886. https://doi.org/10.1038/s41598-023-41103-7.

[8] S. Hernandez, D. Hidalgo,A. Sacco,A. Chiodoni, A. Lamberti, V. Cauda,E. Tresso and Guido Saracco. Comparison of photocatalytic and transport properties of TiO2 and ZnO nanostructures for solar-driven water splitting, Phys. Chem. Chem. Phys., 2015, 17, 7775. https://doi:10.1039/c4cp05857g.

[9] G. Reis, S. Souza, H. Neto, R. Branches, R. Silva, L. Peres, D. Pinheiro, K. Lamy, H. Bencherif and T. Portafaix. Solar Ultraviolet Radiation Temporal Variability Analysis from 2-Year of Continuous Observation in an Amazonian City of Brazil, Atmosphere,2022, 13, 1054. https://doi.org/10.3390/atmos13071054.

[10] Z. Zhang,Y. Song,Y.Xiang and Z. Zhu. Vacancy defect engineered BiVO4 with low-index surfaces for photocatalytic application: a first principles study, RSC Adv., 2022, 12, 31317-25, https://doi.org/10.1039/d2ra04890f.

[11] C.Fu, C., Xu , B., Dong, L., Zhai, J., Wang, X., Wang, D.-Y. Highly efficient $BiVO_4$ single-crystal nanosheets with dual modification: phosphorus doping and selective Ag modification. Nanotechnology, 2021, 32(32). https://doi.org/10.1088/1361-6528/abfc0b.

[12] Y. Qi, J.Zhang, Y. Kong, Y.Zhao, S. Chen, D. Li, W. Liu, Y.Chen, T. Xie, Cui J., C. Li, K. Domen, F. Zhang. Unraveling of cocatalysts photodeposited selectively on facets of BiVO4 to boost solar water splitting. Nature Communications, 2022, 13,484. https://doi.org/10.1038/s41467-022-28146-6.

[13] M. Kaneko, S.Nozawa,Y. Yamashita. Electron-phonon interaction and structural changes in the electronically excited state of WO3 photocatalyst. Frontiers in Energy Research, 2022, 10,1-9. https://doi.org/10.3389/fenrg.2022.933044.

[14] M. Ujihara. The mechanism of water pollutant photodegradation by mixed and core–shell WO3/TiO2 nanocomposites. RSC Advances, 2023, 13(19),12926–12940. https://doi.org/10.1039/d3ra01582c.

[15] A.Aldrees, , H.Khan, A. M Alzahrani, S. Dan'azumi. Synthesis and characterization of tungsten trioxide (WO3) as photocatalyst against wastewater pollutants. Applied Water Science,2023, 13(7), 156. https://doi.org/10.1007/s13201-023-01938-x.

[16] M. Xu, Y.Zhao,Q.Yan. Degradation of aniline by bismuth oxyiodide (BiOI) under visible light irradiation. Journal of Environmental Science and Management, 2017, 20(1), 18–25. https://doi.org/10.47125/jesam/2017_1/03

[17] T. Ke, S.Shen,K. Yang, D. Lin. Construction and visible-light-photocatalysis of a novel ternary heterostructure BiOI/(001)TiO2/Ti3C2. Nanotechnology,2020, 31(34), 345603. http://doi.org/10.1088/1361-6528/ab90ba.

[18] M. Khodamorady, K.Bahrami. A novel ZnS-CdS nanocomposite as a visible active photocatalyst for degradation of synthetic and real wastewaters. Sci. Rep.,2023, 13, 2177. https://doi.org/10.1038/s41598-023-28725-7.

[19] Y.R. Lin, Y.C. Chang, Y.C. Chiao, F.H. Ko. Au@CdS Nanocomposites as a Visible-Light Photocatalyst for Hydrogen Generation from Tap Water. Catalysts, 2023, 13(1):33. https://doi.org/10.3390/catal13010033.

[20] Q. Sun, N. Wang, J. Yu, J. C. Yu. A Hollow Porous CdS Photocatalyst. Advanced Materials, 2018,1804368. https://doi/10.1002/adma.201804368.

[21] M. Sigl, M. Egger, F. Warchomicka, D. Knez, M. Dienstleder,H. Amenitsch, G. Trimmel and T. Rath. ZnIn2S4 thin films with hierarchical porosity for photocatalysis, . Mater. Chem. A, 2024, 12,28965-28974. https://doi/10.1039/D4TA04237A.

[22] Y. Liu, L. Ding,Q.Xu,Y. Maand, J. Hu. Construction of a hierarchical CoP@ZnIn2S4 heterojunction for photocatalytic hydrogen evolution, RSC Appl. Interfaces, 2024,1, 222-232. https://doi/10.1039/d3lf00157a.

[23] X. Yang,L.Zhang,D. Wang,Q. Zhang,J. Zenga and R. Zhang. Facile synthesis of nitrogen-defective g-C3N4 for superior photocatalytic degradation of rhodamine B, RSC Adv., 2021, 11, 30503-30509. https://doi/10.1039/D1RA05535F.

[24] P. Xia, G. Li, X. Li, Sh. Yuan, K. Wang, D. Huang, Y. Ji,Y. Dong, X. Wu, L. Zhu, W. He, and L. Qiao. Synthesis of g-C3N4 from Various Precursors for Photocatalytic H2 Evolution under the Visible Light, Crystals 2022, 12,1719. https://doi.org/10.3390/cryst1212171.

[25] H. Mogi, M. Okazaki, Sh. Nishioka and K. Maeda. In situ formation of a molecular cobalt(III)/AgCl photocatalyst for visible-light water oxidation, Sustainable Energy Fuels,2021, 5, 5694-5698, https://doi.org/10.1039/D1SE01075A.

[26] Y.Bao, K. Chen.AgCl/Ag/g-C_3N_4 Hybrid Composites: Preparation, Visible Light-Driven Photocatalytic Activity and Mechanism, Nano-Micro Lett.,2016, 8(2):182–192, https://doi.org/10.1007/s40820-015-0076-y.

[27] H. Zheng,P. Li,L. Gao and G. Li. Hexagonal AgBr crystal plates for efficient photocatalysis through two methods of degradation: methyl orange oxidation and CrVI reduction, RSC Adv., 2017, 7, 25725-25731. https://doi.org/10.1039/C7RA02354E.

[28] Xiaoyang Yue, Lirong Kong, Xiang Xu, Xiaoping Shen, Xuli Miao, Zhenyuan Ji, Jun Zhu. Synthesis of Ag@AgI plasmonic photocatalyst with enhanced visible-light photocatalytic activity, Desalination and Water Treatment, 2018, 123,156-167. https://doi.org/10.5004/dwt.2018.22653.

[29] Z. Zhou, L. Zhang, W. Su, Y. Li, G. Zhang . Facile fabrication of AgI/Sb2O3 heterojunction photocatalyst with enhanced visible-light driven photocatalytic performance for efficient degradation of organic pollutants in water, Environmental Research, 2021, 197,111143. https://doi.org/10.1016/j.envres.2021.111143.

[30] R. K. Santos, T.A. Martins, G.N. Silva, M. V. S. Conceiçaõ , I.C. Nogueira,E.Longo, G. Botelho. Ag3PO4/NiO Composites with Enhanced Photocatalytic Activity under Visible Light, ACS Omega 2020, 5, 2165121661. https://doi.org/10.1021/acsomega.0c02456.

[31] M. Hagiri, K. Uchida, M. K. Sasaki Sh. Sakinah. Preparation and characterization of silver orthophosphate photocatalytic coating on glass substrate, Scientific Reports, 2021 11:13968. https://doi.org/10.1038/s41598-021-93352-z.

[32] M. Zhou, X. Tian, H. Yu, Z. Wang,C. Ren, L. Zhou, Y.-W. Lin, L. Dou.WO_3 /Ag_2CO_3 Mixed Photocatalyst with Enhanced Photocatalytic Activity for Organic Dye Degradation,ACS Omega,2021, 6, 2643926453. https://doi.org/10.1021/acsomega.1c03694.

[33] S. Ghazi,B. Rhouta, C. Tendero,F. Maury. Synthesis, characterization and properties of sulfate-modified silver carbonate with enhanced visible light photocatalytic performance, RSC Adv., 2023, 13, 23076-23086. https://doi.org/10.1039/d3ra03120a.

[34] W. Zhao, Y. Feng, H. Huang, P. Zhou, J. Lia , L. Zhang, B. Dai, J. Xu, F. Zhu, N. Shenge, D.Y.C. Leung. A novel Z-scheme Ag3VO4 /BiVO4 heterojunction photocatalyst: Study on the excellent photocatalytic performance and photocatalytic mechanism, Applied Catalysis B: Environmental,2019,245, 448-458. https://doi.org/10.1016/j.apcatb.2019.01.001.

[35] L. Gao,Z. Li,J. Liu. Facile synthesis of Ag3VO4/b-AgVO3 nanowires with efficient visible-light photocatalytic activity, RSC Adv., 2017, 7, 27515-27521. https://doi.org/10.1039/c7ra03955g.

[36] W. Li, Qianlin Chen, X. Leia and Sh. Gong. Fabrication of Ag/AgBr/Ag3VO4 composites with high visible light photocatalytic performance, RSC Adv., 2019, 9, 5100-5109. https://doi.org/10.1039/c8ra10538c.

[37] Y. Hara, T. Takashima, R. Kobayashi, S. Abeyrathna, B. Ohtani, H. Irie. Silver-Inserted Heterojunction Photocatalyst Consisting of Zinc Rhodium Oxide and Silver Antimony Oxide for Overall Pure-Water Splitting under Visible Light, Applied Catalysis B: Environmental, 209, 663–668. https://10.1016/j.apcatb.2017.03.040.

[38] M.J.Islam, A.Kumer. First-principles study of structural, electronic and optical properties of AgSbO3 and $AgSb_{0.78}Se_{0.22}O_3$ photocatalyst. SN Appl. Sci. 2, 251 (2020). https://doi.org/10.1007/s42452-020-2058-z.

[39] Z. Lou,B. Huang,Z. Wang,X. Ma,R. Zhang,X. Zhang,X. Qin,Y. Dai,M.-H.Whangbo. Ag6Si2O7:a Silicate Photocatalyst for the Visible Region. Chemistry of Materials,2014, 26(13), 3873–3875. https://10.1021/cm500657n.

[40] Z. Yi, J.Ye, N.Kikugawa, T. Kako, Sh. Ouyang, H. Stuart-Williams,H. Yang, J. Cao, W. Luo, Z. Li, Y. Liu, R. L. Withers. An orthophosphate semiconductor with photooxidation properties under visible-light irradiation. Nature Mater,2010, 9(7), 559–564. https://doi.org/10.1038/nmat2780.

[41] P. Giannozzi, O. Baseggio, P. Bonfà, D. Brunato, R. Car, I. Carnimeo, C. Cavazzoni, S. de Gironcoli, P. Delugas, F. Ferrari Ruffino, A. Ferretti, N. Marzari, I. Timrov, A. Urru, S. Baroni. Quantum ESPRESSO toward the exascale,J. Chem. Phys,2020, 152, 15, 154105. https://doi.org/10.1063/5.0005082.

[42] M.J. van Setten, M. Giantomassi, E. Bousquet, M.J. Verstraete, D.R. Hamann,X. Gonze, G.-M. Rignanese. The PseudoDojo: Training and grading a 85 element optimized norm-conserving pseudopotential table, Computer Physics Communications,2018, 226, https://doi.org/10.1016/j.cpc.2018.01.012.

[43] Perdew, J. P., Burke, K., Ernzerhof, M. Generalized Gradient Approximation Made Simple. Phys. Rev. Lett., 1996,77, 3865–3868. https://doi.org/10.1103/PhysRevLett.77.3865.

[44] J. P. Perdew, K. Burke, and M. Ernzerhof,Generalized Gradient Approximation Made Simple,Phys.Rev.,Lett.77,3865. https://doi.org/10.1103/PhysRevLett.77.3865.

[45] Leopold Talirz, Snehal Kumbhar, Elsa Passaro, Aliaksandr V. Yakutovich, Valeria Granata, Fernando Gargiulo, Marco Borelli, Martin Uhrin, Sebastiaan P. Huber, Spyros Zoupanos, Carl S. Adorf, Casper Welzel Andersen, Ole Schütt, Carlo A. Pignedoli, Daniele Passerone, Joost VandeVondele, Thomas C. Schulthess, Berend Smit, Giovanni Pizzi Nicola Marzari.Materials Cloud, a platform for open computational science. Sci Data,2020, 7, 299. https://doi.org/10.1038/s41597-020-00637-5.

[46] J.Bardeen, W. Shockley. Deformation potentials and mobilities in non-polar crystals, Phys. Rev.,1950,80, 72. https://doi.org/10.1103/PhysRev.80.72.

[47] R.W.G. Wyckoff. Crystal structure of silver phosphate and silver arsenate (ag3 x o4). American Journal of Science, 1925, Serie 5(1,1921-1938), 10, 107–118.

[48] A. Durif, I.Tordjmax,R. Masse (1976). Affinement de la structure cristalline du monophosphate d'argent Ag3PO4. Existence d'une forme haute témperature. Zeitschrift Für Kristallographie - Crystalline Materials, 1976,144,1-6. https://10.1524/zkri.1976.144.16.76.

[49] T.Katsura, Y. Tange. A Simple Derivation of the Birch–Murnaghan Equations of State (EOSs) and Comparison with EOSs Derived from Other Definitions of Finite Strain, Minerals, 2019, 9(12), 745. https://doi.org/10.3390/min9120745.

[50] Y. Lu, Sh. Zhu, E.Huang,Y.He,H. Yan. Pressure-driven band gap engineering in ion-conducting semiconductor silver orthophosphate, J. Mater. Chem. A, 2019, 7,4451-4458, https://doi.org/10.1039/C8TA10606A.

[51] N.Umezawa,O. Shuxin,J. Ye. Theoretical study of high photocatalytic performance of Ag3PO4, Physical Review B, 2011, 83(3), 035202. https://doi.org/10.1103/PhysRevB.83.035202.

[52] F. Lipsky,L. H.S. Lacerda, S. R. Lazaro, E.Longo, J.Andrés and M. A. San-Miguel. Unraveling the relationship between exposed surfaces and the photocatalytic activity of Ag3PO4: an in-depth theoretical investigation, RSC Adv., 2020, 10, 30640-30649. https://doi.org/10.1039/d0ra06045c.

[53] R. Sinha,D. Friedrich, G. Zafeiropoulos, E. Zoethout, M. Parente, M. C M van de Sanden, A. Bieberle-Hütter. Charge carrier dynamics and photocatalytic activity of 111 and 100 faceted Ag3PO4 particles, J. Chem. Phys. 2020, 152, 244710. https://doi.org/10.1063/5.0006865.

[54] Timoshevskii, S. Kotrechko, and Yu. Matviychuk. Atomic structure and mechanical properties of carbyne, 2015, Physical Review B 91(24). https://doi.org/10.1103/PhysRevB.91.245434.

[55] Y.Xu , M.M.M.Schoonen.The absolute energy positions of conduction and valence bands of selected semiconducting minerals. American Mineralogist, 2000,85, 543-556. https://doi.org/10.2138/am-2000-0416.

[56] H. Dong,J. Sun,G. Chen,Ch. Li,Y. Hua and Ch. Lv, An advanced Ag-based photocatalyst Ag2Ta4O11 with outstanding activity, durability and universality for removing organic dyes, Phys. Chem. Chem. Phys., 2014, 16, 23915-23921, https://doi.org/10.1039/C4CP03494E.

[57] X. Ma, B. Lu, D. Li, R. Shi, Ch. Pan, and Y.Zhu. Origin of Photocatalytic Activation of Silver Orthophosphate from First-Principles, J. Phys. Chem. C 2011, 115, 4680–4687. https://doi.org/10.1021/jp111167u.